Nuclear Materials and Energy 45 (2025) 101998

Contents lists available at ScienceDirect

Nuclear Materials and Energy

journal homepage: www.elsevier.com/locate/nme

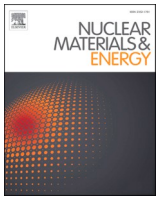

Evolution of elemental depth profiles on co-deposited layers at the divertor region of the WEST tokamak during its Phase 1 operations☆

A. Hakola [a,*], J. Likonen [a], T. Vuoriheimo [b], E. Grigore [c], I. Jõgi [d], P. Paris [d], A. Lagoyannis [e], K. Mergia [e], P. Tsavalas [e], E. Fortuna-Zaleśna [f], M. Balden [g], E. Bernard [h], M. Diez [h], E. Tsitrone [h], the WEST team [1]

[a] VTT, Espoo, Finland
[b] Department of Physics, University of Helsinki, Helsinki, Finland
[c] National Institute for Laser, Plasma and Radiation Physics, Bucharest, Romania
[d] University of Tartu, Institute of Physics, Tartu, Estonia
[e] National Centre for Scientific Research "Demokritos", Athens, Greece
[f] Warsaw University of Technology, Warsaw, Poland
[g] Max-Planck-Institut für Plasmaphysic, Garching, Germany
[h] CEA, IRFM, F-13108 Saint-Paul-Lez-Durance, France

ARTICLE INFO

Keywords:
Deposited layer
WEST
Divertor
Boronization
Marker tile

ABSTRACT

We discuss detailed elemental, compositional, and structural properties of co-deposited layers formed on the special marker tiles at the divertor region of the WEST tokamak during its Phase 1 (2016–2021) plasma operations. The main new aspects are applying high depth and mass resolution, provided by a combination of state-of-the-art local analysis techniques, throughout the entire surface deposit and cross correlating the obtained results with published ones. We also show that proper comparison of the different data sets requires deconvoluting them with several experimental parameters, most importantly the lateral and depth resolutions as well as the analysis volume. The analyses reveal that the thickest deposits are formed towards the end of Phase 1, and the change is particularly noticeable after the C4 campaign with the longest exposure time and the largest number of boronizations carried out. Thin deposits (thickness up to 1–2 μm) are found on several poloidal regions of the analysed tiles, and they exhibit a clear sandwich-type of structure consisting of distinct B, C, O, and/or W-rich sublayers together with metallic impurities. Close to the inner strike point, thick deposits are measured (thickness several tens of micrometres) and they show complex, stratified structures, however, the same sublayer structure as for the thin deposits can still be recognized. On the thin deposits, the very surface is rich in B while for the thick deposits W dominates the topmost surface layers in the latter stages of Phase 1. For all the analysed samples, the superficial B and W concentrations are on average 10–30 at.% in addition to which high oxygen levels up to 15–40 at.% are measured. In the erosion-dominated regions, deposits can be observed but only in the microscopic scale inside recessed valleys, up to thicknesses of several micrometres. A dynamical erosion–deposition picture for the surface layers is confirmed, further contributing to their structure and composition.

1. Introduction

Migration of material in the scrape-off layer (SOL) plasma can lead to the formation of complex co-deposited layers on plasma-facing components (PFCs) in specific regions of tokamak-type fusion reactors [1]. Such layers typically consist of material eroded from the PFCs, various impurity elements as well as plasma fuel. Thorough understanding of their composition, thickness, and formation mechanisms will help in controlling the lifetime of PFCs as well as minimizing the production of dust and retention of radioactive tritium (T) in the reactor vessel.

☆ This article is part of a special issue entitled: 'PFMC-20' published in Nuclear Materials and Energy.

* Corresponding author.
E-mail address: antti.hakola@vtt.fi (A. Hakola).

[1] See http://west.cea.fr/WESTteam.

https://doi.org/10.1016/j.nme.2025.101998
Received 14 July 2025; Received in revised form 30 August 2025; Accepted 30 September 2025
Available online 2 October 2025
2352-1791/© 2025 The Authors. Published by Elsevier Ltd. This is an open access article under the CC BY-NC license (http://creativecommons.org/licenses/by-nc/4.0/).

In recent years, material migration and the properties of the co-deposits have been investigated in detail in metallic fusion devices, including JET [2], ASDEX Upgrade (AUG) [3], EAST [4], and WEST [5]. Of these, WEST is a particularly interesting testbed since it allows studying plasma-wall interaction (PWI) phenomena in an ITER-relevant full-tungsten (W) environment during long plasma pulses, up to more than 20 min [6]. WEST has been in operation during two distinct experimental periods: Phase 1 (in 2016–2021) and Phase 2 (since 2022). In the lower divertor region, W-coated graphite PFCs were used throughout Phase 1 while for the Phase 2 operations, ITER-grade PFCs with a W monoblock structure were installed .

This contribution focuses on divertor tiles removed for surface analyses from WEST after individual campaigns during Phase 1. More specifically the results have been extracted from special *marker tiles*, equipped with thin W and molybdenum (Mo) layers on top of the standard coated PFCs for detailed studies of *campaign-integrated net erosion and deposition*. Previous results from marker tiles have revealed us [5–9].

- characteristic regions poloidally in different parts of the divertor, ranging from erosion-dominated parts to areas with co-deposited layers of varying thicknesses;
- deposition becoming much more prominent with increasing plasma exposure, in particular after initiating boronizations on WEST;
- erosion and deposition profiles showing notable variations in the toroidal direction, driven by the strong magnetic ripple on WEST; and
- especially the thickest deposits manifesting a complicated structure, reflecting the versatile exposure history of the divertor PFCs.

Here we will cast more light on the detailed structure of the deposits and aim at identifying differences in their composition and structure with increasing campaign time. The results will also be compared to the available literature data [5–12]. We will discuss the behaviour of elemental depth profiles in the deposits and extract information on the campaign-integrated amounts of key impurities (such as boron (B) and carbon (C)) and the plasma fuel deuterium (D) on the PFC surfaces in different length scales from a few mm down to the μm level. In addition, the high depth and mass resolution, offered by state-of-the-art local analysis methods, will provide us with new insights into how material has accumulated not only at the very surface but throughout the entire deposit. At the same time, we will highlight that proper comparison of the measurement results requires deconvoluting the obtained data sets with several experimental parameters, most importantly the lateral and depth resolutions as well as the applied analysis volume. The main parametric dependencies investigated in this work are the exposure time of the PFCs (tiles removed after successive campaigns for analyses), poloidal location along the divertor surface (on samples extracted from the removed tiles at pre-determined locations), analysis depth (from a few nm down to tens of micrometres), analysis area (from sub-μm to mm-sized spots), and depth resolution (from a few to several hundreds of nm).

2. Experimental

2.1. WEST campaigns during Phase 1 (2016–2021)

The Phase 1 of WEST consisted of 5 experimental campaigns (labelled as C1-C5, no plasmas performed in C1). The details of the campaigns are shown in Table 1. Overall, the PFCs experienced more than 7 h of cumulative plasma exposure until the end of C5, mainly in L-mode or ohmic plasma conditions. A significant number of transients were recorded, and a considerable share of the discharges in each campaign ended in a disruption. External heating was performed by Lower Hybrid Current Drive (LHCD) and Ion Cyclotron Resonance Heating (ICRH), the latter from C3 onwards. Especially in C4 and C5, the surface temperature of the divertor PFCs rose up to 1000 °C while in C3, more moderate values with a maximum of 500 °C were measured. Boronizations were started during C3, but they were most regularly applied during C4 [8]. Finally, a dedicated He campaign was executed in the very end of C4 as discussed in [9]. Worth noticing is the large radiated power fraction of >50 % in discharges throughout Phase 1, which set strict requirements for scenario optimization.

2.2. Analysed marker tiles and their characteristic erosion and deposition regions

Altogether 8 marker tiles were mounted on the WEST divertor before Phase 1 as illustrated in Fig. 1. Both at the high-field (inner, HFS) and low-field (outer, LFS) side, the toroidal positions of six of them were selected such that the tiles would coincide with the maxima of the magnetic ripple. For comparison, two marker tiles, one at HFS and the other at LFS, were mounted at the minima of the toroidal ripple; Analyses of these tiles is still pending while the impact of toroidal ripple in general has been reported in [13]. Fig. 1 also shows how the marker tiles were sequentially removed after each campaign phase C3, C4, and C5, respectively. Note that there are two tiles in each toroidal location in Fig. 1: one at the HFS, the other at the LFS.

The marker tiles had a 1–2 μm thick W coating together with a thin Mo (~0.1 μm) interlayer on standard WEST PFCs. The standard PFCs, for their part, showed a 12-μm thick W coating and a thinner Mo intermediate layer (~3.5 μm) on graphite. Standard coatings had been prepared using a combination of magnetron sputtering and ion implantation [14] while arc-discharge deposition was applied for the marker coatings [15].

Based on earlier investigations (see [5,7]), characteristic erosion and deposition patterns have been measured along the poloidal direction as illustrated in Fig. 2. The *s* coordinate starts from the innermost corner of the HFS divertor and runs along the divertor surfaces poloidally to the outermost point of the LFS divertor.

- *Erosion-dominated areas* close to the inner strike point (ISP) and outer strike point (OSP), highlighted in yellow. The exact locations vary from campaign to campaign but typically the ISP region is ~ 40–50 mm wide around $s \sim 250$ mm while the OSP area is more extended (starting from $s \sim 330$ mm and extending by 100–120 mm), starting from the inner edge of the outer-divertor tile.

Table 1
Overview of the campaigns carried out in Phase 1 of WEST: number of plasma discharges performed, cumulative plasma time, number of disruptions, total LHCD and ICRH energy for heating, and number of boronizations.

Campaign & schedule	Plasma discharges	Plasma time (s)	Disruptions	$W_{LHCD,tot}$ (MJ)	$W_{ICRH,tot}$ (MJ)	Boronizations
C2 Nov17-Feb18	716	1553	282	95.5	0	0
C3 July-Dec18	1076	7329	796	4947	105	3
C4 July-Nov19	1442	12,669	1042	12,123	1142	13
C5 Nov20-Jan21	655	4630	460	2625	182	2

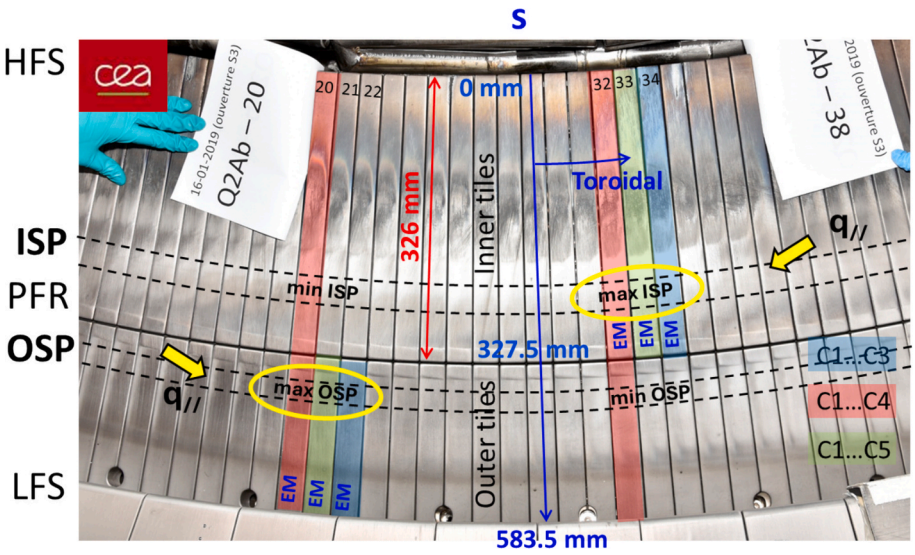

Fig. 1. Photograph of the WEST divertor sector, highlighted with the locations of the marker tiles (EM) during the 2019 opening. The poloidal s coordinate starts from the innermost HFS corner and runs along divertor surfaces towards LFS. The direction of the parallel heat flux has been marked together with the maxima and minima of the toroidal ripple. Tiles marked in blue were removed after C3, those in red after C4, and the green ones after C5. Figure adopted from [7] and re-drawn. Each toroidal position (20–22 and 32–34 highlighted in the figure) contains two tiles: one at the HFS (from s = 0 to 326 mm), the other at the LFS (from s = 327.5 to 583.5 mm).

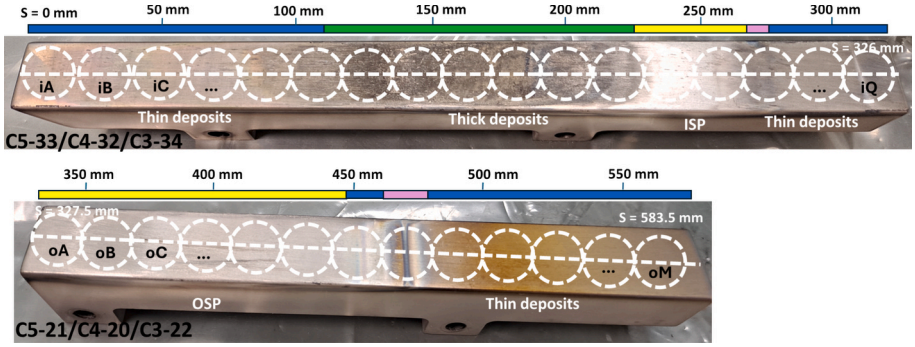

Fig. 2. Photographs of marker tiles C5-33i and C5-21o removed after the C5 campaign. The approximate locations of the characteristic regions are denoted by the color bars on top of the photos. The rainbow-colored layers are highlighted in magenta, other thin deposits in blue, thick deposits are denoted by green, and erosion-dominated areas are marked in yellow. This colour-coding scheme is also used in the later figures. The white dashed lines indicate the central lines of the tiles (in the toroidal direction) as well as the locations of the samples drilled from each marker tile. The naming scheme for the inner-divertor samples is the following: C5-33/C4-32/C3-34iA, iB, iC,…, iQ denoting the samples taken from tiles after the C5/C4/C3 campaigns. The corresponding one for the outer-divertor samples is C5-21/C4-20/C3-22oA, oB, oC,…,oM.

- *Thick deposits* (thicknesses up to tens of μm, see section 3) next to the ISP on the SOL side (marked in green) and the thickest layers concentrating around $s \sim 100$–200 mm.
- *Thin deposits* (thicknesses < 1–2 μm, see section 3 for details) both on the HFS ($s \sim 0$–110 mm & 270–320 mm) and LFS ($s \sim 450$–580 mm) tiles denoted by blue in the colour bar. On narrow zones both at the private flux region (PFR) and on the SOL side of the OSP – marked in magenta – the deposits are particularly prominent with a rainbow-coloured appearance, showing sharp transition from net erosion to deposition (within a range of < 5 mm). Deep in the PFR and in the peripheral regions, the deposited layers, in contrast, are almost non-existent.

The analyses discussed hereafter are taken from small cylindrical samples (diameter 17 mm, height 10 mm), extracted by core drilling from the different marker tiles poloidally along the central line (see Fig. 2). Overall 17 and 13 samples were taken from each inner and outer divertor tile, respectively after each campaign. The analyses were performed on multiple locations of the selected samples to obtain a detailed picture of layers formed on the regions described above and to increase the statistics of the analyses. The locations of the samples extracted from the tiles can be found in Fig. 2 in terms of the *s* coordinate used. Different sets of samples were used in different analyses (see details in section 2.3 and Table 2) but due to the large number of samples (30 samples for each campaign and 3 campaigns altogether), it was decided not to use the sample nomenclature in this paper but rather discuss the results in terms of deposition/erosion areas.

2.3. Surface analyses made on marker tiles

The results reported in this article are based on data extracted from measurements by the following surface-analysis techniques: (i) Secondary Ion Mass Spectrometry (SIMS), (ii) Glow Discharge Optical Emission Spectroscopy (GDOES), (iii) Laser Induced Breakdown Spectroscopy (LIBS), (iv) Nuclear Reaction Analysis (NRA) and Rutherford Backscattering Spectrometry (RBS), (v) static X-ray Photoelectron Spectroscopy (XPS), and (vi) Scanning Electron Microscopy (SEM) with Energy Dispersive X-ray analysis (EDX) assisted by Focused Ion Beam

Table 2
Overview of the samples analyzed by each contributing method together with their main features in the series of measurements performed for the WEST samples. The maximum depth as well as the depth and lateral resolutions are valid for the measurements of the present sets of samples.

	SIMS	GDOES	LIBS	NRA/RBS	XPS	SEM/EDX
Samples analysed	C3-34iB, F, K, M, Q	C3-34iF, I, O	C4-32iA, H, N, P	C3-34iQ	C3-34iF, I, O	C3-34iC, J, L
	C4-32iB, E, K, M, Q	C4-32iF, O	C4-20oC, L	C4-32iQ	C4-32iF, I, O	C4-32iC, J, L
	C5-33iB, E, K, M, Q	C5-33iF, O		C5-33iQ	C5-33iF, I, O	C5-33iC, J, L
	C3-22oB, E, G, J	C3-22oA, I, M		C3-22oB, G	C3-22oA, I, M	C3-22oF, H, K
	C4-20oB, E, G, JC5-21oB, E, G, J	C4-20oA, I, M		C4-20oB, G	C4-20oA, I, M	C4-20oF, H, K
		C5-21oA, I, M		C5-21oB, G	C5-21oA, I, M	C5-21oF, H, K
Max depth (μm)	~20	>20	No limit	~3	0.01	No limit (w/ FIB)
Analysis area (mm^2)	~0.1	12.5	~0.4	~7	~1	Down to sub-μm features
Depth resolution (nm)	~1 (surface), <100 deep inside	<100	<1000	<50	<10	<100 (w/ FIB)
Lateral resolution (mm)	<5	~20	<5	~3	~1	No limit (w/ FIB)

(FIB) cross sectioning. The first four methods provide elemental depth profiles at varying resolutions (from some nm in SIMS and GDOES to hundreds of nm in LIBS) and analysis depths (from a few μm in NRA to 10–20 μm in SIMS and to the entire pile of deposits and coatings in GDOES and LIBS). One should note, however, that the quoted depth resolutions are only valid at the surface: Deeper inside, the results will be smeared out by concurrent signal yields from different depths.

The key features of the different analysis method are collected in Table 2 together with the list of samples analyzed by each of them. The measurements were typically scheduled such that the most destructive ones (SIMS, LIBS, GDOES) could be made the last if the very same samples were analyzed by multiple techniques. An exception were the NRA/RBS measurements that were carried out after the SIMS analyses. In any case, sufficient space was always left on the sample surface after any analysis was completed such that the next measurements would not be affected by the surface modifications that the previous step would have induced.

The main elements of interest are D, B, C, oxygen (O), as well as Mo and W from the marker layers. In addition, other major impurities like nitrogen (N, from vents and plasma experiments), copper (Cu, from LHCD antennas), and iron (Fe, originating from steel structures of the vessel) are profiled. Integration over relevant peaks in the depth profiles at each measurement point will provide us with qualitative deposition profiles along the desired direction that can be further converted into surface densities (in at/cm^2) or relative concentrations (in at. %) by proper calibration, thus allowing comparison to the data in [5–12].

The SIMS measurements were performed using a double focusing magnetic sector instrument (VG Ionex IX-70S) [16], for the GDOES measurements a GDA 750 instrument was utilized [17], while the LIBS measurements were carried out according to the procedure described in [11,19]. The analysis area was 0.3 × 0.4 mm^2 in SIMS; in GDOES, for its part, a circular spot with the area of ~12.5 mm^2 was used, while the diameter of the approximately circular LIBS crater was 0.7 mm. NRA/RBS investigations were made using a D beam (energy 1.6 MeV) with a diameter of 2–3 mm, ensuring an analysis depth of ~3 μm [18]. For estimating the elemental contents of different elements in the entire deposit or the marker-layer structure, the NRA/RBS results need to be extrapolated throughout the entire thickness of the deposit by assuming that the elemental concentrations remain constant beyond the maximum accessible depth. One should note that the varying analysis volumes automatically led to different levels of averaging during the measurements.

Of the other methods, static XPS gives atomic and chemical information on the very surface (5–10 nm) while SEM/EDX provides overviews on both the morphology of the surface and cross sections of the deposits after performing FIB cuts on targeted regions on the PFC surface. In XPS, an Escalab Xi spectrometer with the Al K_α radiation (1486.6 eV) and the analysis area of ~1 mm^2 was used, whereas for the SEM/EDX measurements several different devices were selected, including a ThermoFisher Scientific Apreo2 field-emission SEM together with an Oxford Instruments ULTIM-MAX EDX and a Hitachi SU-8000 field-emission SEM combined with a ThermoFisher Scientific Ultra Dry EDX both with a FIB cutting option.

3. Results and discussion

3.1. Elemental depth profiles for deposits on the marker tiles

All the characteristic regions of Fig. 2 show strongly varying depth profiles for the main analysed elements D, B, C, and O as well as for other metallic and non-metallic impurities. Examples from GDOES and LIBS profiles after the C3, C4, and C5 campaigns are collected in Fig. 3 while corresponding SIMS and NRA/RBS profiles can be seen in Fig. 4.

3.1.1. Overview of GDOES and LIBS profiles

The GDOES results give an overview on how successive Mo and W layers on graphite have evolved during the Phase 1 operations. On the *thin-deposit region* (see the profiles at s = 104–105 mm, Fig. 3(a1) and (a2)), the markers largely follow their original specifications while thicker deposited layers can be identified on the top surface, resulting in, e.g., the peak for the first Mo marker moving towards larger depth values (from ~1.5 μm to ~1.8 μm) from C3 to C5 and becoming less and less pronounced; The latter is likely due to degraded resolution of GDOES deeper inside the deposit [16]. Extracting data from the area of *thick deposits* was challenged by the rough and uneven surface of the analysed samples, up to the point that no reliable GDOES measurements were possible in these regions after C4 and C5. In the *erosion zone* (example profiles at s = 340–341 mm, Fig. 3(b1) and (b2)), the thicknesses of the different W and Mo coatings are clearly reduced, and already after C4, the markers become hardly identifiable. Concerning the actual surface deposits, GDOES gives only a rough estimate for their composition and predicts low values for, e.g., the C and B contents of the layers compared to the other analysis methods.

The in-depth discussion of the LIBS results can be found in [19] while Fig. 3(c)-(g) shows normalized (with respect to the W signal) B, O, Cu, and Mo depth profiles for pre-selected spectral lines within the first 1–2 μm (30 laser pulses) on samples extracted from different characteristic regions. Generally, the depth profiles for B and Mo agree reasonably well with the GDOES and SIMS results in the region of the thinnest deposits (s < 100 mm or > 500 mm, parts (c) and (g)) while the match is far from perfect for any thicker surface films. However, one should note that due to a large ablation rate of 50–100 nm/pulse or even hundreds of nm/pulse for the thick deposits, the depth resolution of LIBS is not that high as is the case for SIMS or even NRA/RBS. Nevertheless, LIBS is particularly useful in identifying the extent of a superficial B-rich layer, with its thickness ranging from a few nm in the peripheral regions to several micrometres for samples drilled from the areas of thick deposits. In the erosion-dominated zones, measurable deposited layers are present close to the ISP (s = 255.5 mm, Fig. 3(e), see discussion in section 3.2) while in the vicinity of the OSP (s = 375.5 mm, Fig. 3(f)), a more traditional picture of remnants of different impurity elements on the surface becomes evident.

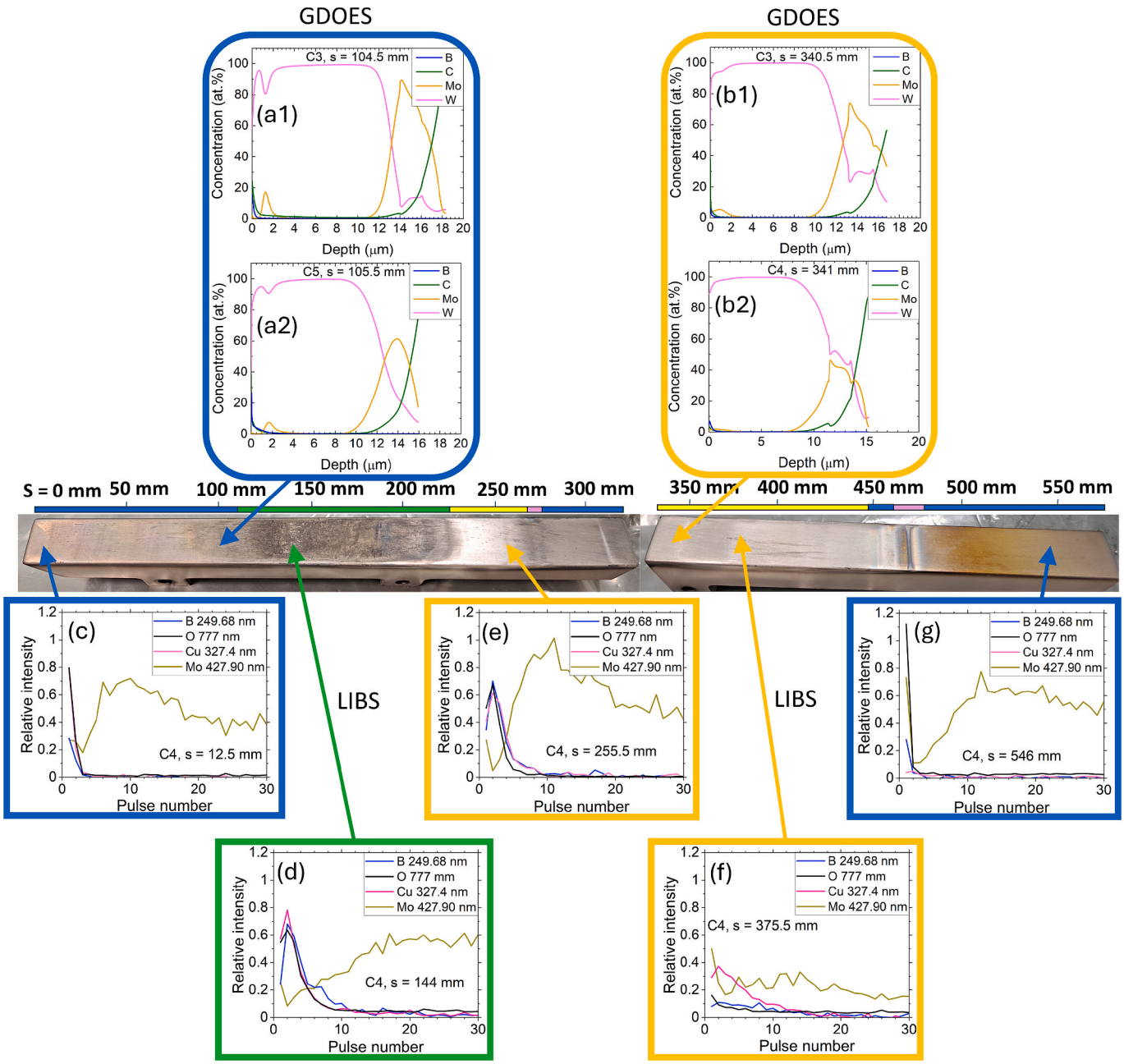

Fig. 3. Selected GDOES (a1, a2, b1, b2) and LIBS (c-g) depth profiles from different characteristic regions (thick deposits (green), erosion areas (yellow), thin deposits (blue, purple)) after the C3, C4, and C5 campaigns. Parts (a1) and (b1) are measured after C3, parts (b2) and (c-g) after C4, while (a2) is taken after C5.

3.1.2. Analysis of the SIMS depth profiles

In this section we will concentrate on the SIMS depth profiles and make comparisons with the NRA/RBS data extracted from the same samples. The measurement depth has been determined such that either the first Mo marker is reached or that the surface signals have saturated to their background values. The apparent decrease of the W profile within the W marker or in the 12-μm thick standard coating on some of the example plots of Fig. 4 (e.g., in the $s = 199$ mm plot after C3, Fig. 4 (a1)) is an artefact due to (i) strong matrix effects, leading to different W yields from successive layers; (ii) attenuation of the signal originating from the ever-deepening SIMS crater; and (iii) occasional drifting of the signals with respect to the electronic measurement gate. Concerning points (ii) and (iii), all the elemental mass signals were similarly affected and thus introduced no additional errors to the interpretation of the data. In the following, we will discuss results obtained from each characteristic region according to Fig. 2 separately.

Thin deposits. The thickness of these layers ranges from a few nm (deep in the PFR and in the peripheral zones on the LFS SOL) to ~1 μm in the rainbow-coloured regions; Of the latter examples are shown around $s = 452$–455 mm in Fig. 4(c1)-(c3). A distinguished sublayer structure can be identified, evidenced by the maxima for B, C, Fe, and Mo occurring at different depths within the first micrometre; Particularly well the sublayers are visible on the C4 and C5 samples (at $s = 452.5$ mm, Fig. 4(c2) and (c3)). The very surface (in the example profiles ~200–300 nm) is dominated by boron and, as NRA (and LIBS) measurements indicate, also by oxygen. On some samples, mainly in the PFR and poloidally far away from the strike points, B is accompanied with distinct C and D peaks but the thicker the layer becomes, the more clearly the C and D maxima occur a bit deeper (typically 50–100 nm) inside the B-rich layer. Also W is prominently present, accounting for 5–55 at.% of the composition of the layers according to the accompanying NRS/RBS depth profiles at $s = 450$ mm (Fig. 4(d1)-(d3)).

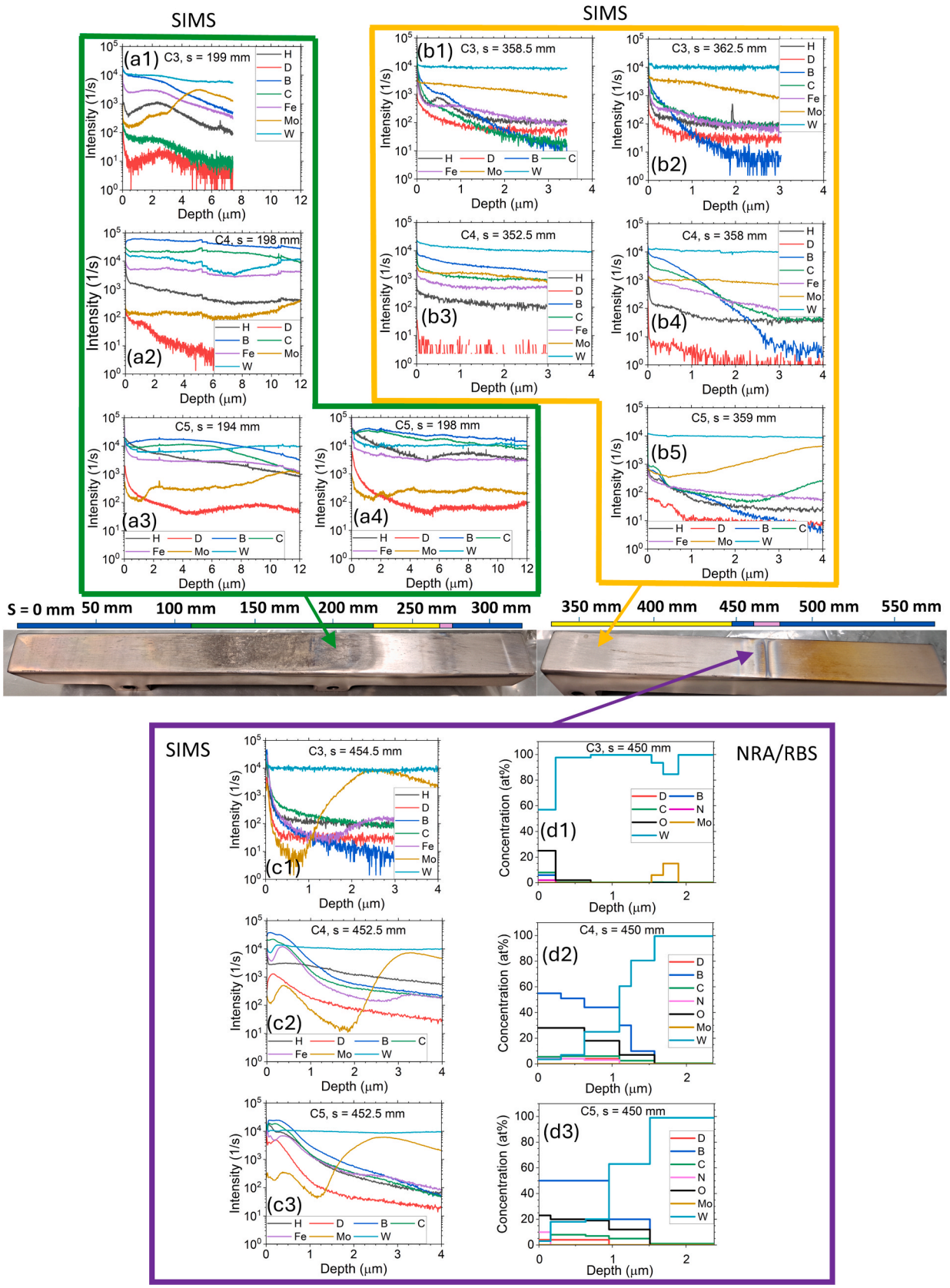

Fig. 4. Selected SIMS (a1-a4, b1-b5, c1-c3) and NRA/RBS (d1-d3) depth profiles from different characteristic regions (thick deposits (green), erosion areas (yellow), thin deposits (blue, purple)) after the C3, C4, and C5 campaigns. Parts (a1), (b1), (b2), (c1), and (d1) are from C3 samples, parts (a2), (b3), (b4), (c2), and (d2) recorded after C4, and finally parts (a3), (a4), (b5), (c3), and (d3) after C5.

The next characteristic region (from ~200 nm to ~400 nm in Fig. 4 (c2) and (c3)) contains several metallic impurities such as Fe and Mo but also Cu (not analysed by SIMS but verified by SEM/EDX analyses, see section 3.2), originating from the steel structures (Fe, Mo) and LHCD antennas (also Cu) of WEST. Notice however that SIMS is very sensitive to these elements, thus the main constituents of the second layer are still B, O, and W. At the same time the W concentration increases until the underlying marker-layer configuration (W + Mo) is reached (at ~800–1000 nm). The latter point is marked by all the impurity elements having decreased by 50 % from their peak values and W originating from the coating is left. According to NRA analyses, the O concentrations are at a high level of 20–30 at.% throughout the deposits, not just in the very surface.

It is worth noting that the depth profiles presented in Fig. 4 have resulted from averaging over several thinner sublayers within the co-deposits, below the depth resolution of SIMS. Nevertheless, at least for the above-mentioned rainbow-coloured deposits, the outcome is not just continuous piling up of material on the existing surface but multiple erosion-migration-deposition-boronization cycles have impacted the structure and elemental content of the layers throughout the experimental campaigns. This is evidenced by the fact that especially after C4 and C5, the films are qualitatively comparable and do not show additional archaeological layers deeper inside the deposits. It is of course possible that due to the short duration of the C5 campaign, most erosion and deposition patterns encountered on the C5 marker tiles actually reflect the outcomes of the C4 campaign, thus providing an alternative explanation to the similarities mentioned above.

Thick deposits. The thick deposits cover a range from a few to several tens of micrometres and even in adjacent measurement locations show notable local variations in their thickness as well as for the shapes of the SIMS depth profiles (see Fig. 4(a1)-(a4) for the profiles at $s \sim$ 194–198 mm). As will be discussed in section 3.2, the deposits are stratified structures, consisting of multiple sublayers, and the elemental depth profiles shown in Fig. 4 will therefore be a convolution of several finer details with decreasing depth resolution as one proceeds deeper inside the deposits.

Generally, the main elements that can be recognized are B, C, O, and W – as is the case for the thin deposits – and metallic impurities. The cyclic nature of erosion and deposition processes as proposed for the thin deposits could have impacted the formation of the layers but now the balance is much more towards net deposition than is the case for other analysed regions. The depth profiles are relatively flat for all the recorded masses, showing that on average the surface films are not noticeably enriched in any of the recorded elements. However, since the sublayers evolve rapidly (see discussion in section 3.2) in the toroidal and poloidal directions – both by their thickness and by how much they are additionally modified by, e.g., chemical reactions, partial delamination, and arcing – SIMS with its large analysis area cannot reveal all the fine details on the studied samples. The deuterium inventories exhibit even stronger local variations than is the case for the other studied elements: from almost non-existent to peaked ones at the surface and finally to uniform profiles indicating large fuel inventories in the deposited layers. One possible explanation for the seemingly random behaviour comes from the fact that the analyses were carried out close to the ISP ($s \sim$ 200 mm), which might have induced local desorption of the retained fuel particles. Indeed, control measurements from standard coated tiles further away from the ISP ($s \sim$ 150–170 mm, data not shown here) indicate practically constant D levels within the same depth range where also the B and C signals reach their maxima. This is in accordance with the observations in [5,7].

The underlying W and Mo markers in the SIMS data are somewhat challenging to be distinguished from surface layers and even from each other, as is typically the case for rough or strongly modified surfaces. On the other hand, concerning only the surface deposits, their thickness consistently increases from C3 to the subsequent campaigns. After C3, W is the most prominent signal while during C4 and C5, more and more B and C is accumulated in the layers. Depending on the poloidal coordinate, B and C can be constantly present in the entire deposit but more typically the first couple of hundreds of nm is a W-rich region while the light impurities peak only deeper inside, at a depth of some micrometres. This is a qualitative difference from the dominating trend for the thin deposits, though partly being affected by the tendency of the thickest deposits to flake off.

Erosion regions. In these areas no clearly defined surface deposits can be identified but typically a collection of different elements closest to the surface – W and Mo from the markers and traces of B, C, and O. This apparent mixture of elements is largely influenced by averaging across neighbouring regions with strongly varying compositions. The surface changes even more rapidly poloidally or toroidally than is the case for the thin or thick deposits: within a few mm, a potpourri of features from almost complete erosion of all the markers to accumulation spots for re-deposited material with thicknesses up to some micrometres and everything in between can be recognized. Examples have been collected from the OSP region s = 352.5–362.5 mm in Fig. 4(b1)-(b5), from close-by measurement points after C3 and C4. Data from the ISP region, instead, can be found in [22], and together with the SEM data (section 3.2) and SIMS control measurements from standard tiles (not shown), the extent of the actual net-erosion area on the inner side is very narrow and the depth profiles are comparable to the ones taken from the region with the thinnest deposits, at least locally.

3.2. Cross sections of the deposited layers

The cross-sectional SEM and FIB images in Fig. 5 give additional support for the statements put forward in section 3.1.

In the region of *thin deposits*, B-, C-, and/or W-rich sublayers can be identified on the surface before the W marker is reached (see Fig. 5(a) at s = 433 mm). Based on EDX analyses, oxygen is prominently present in the deposits together with metallic impurities, most notably Cu except for sublayers almost exclusively consisting of W (point #2 as an example). Local erosion of protruding surface features is visible, and the eroded material has re-deposited in recessed regions on the same sample, with the phenomena becoming most pronounced after C4 and C5. At the outer divertor, signs of re-solidified molten material can be noticed in the sediments, indicative of arcing, as well as noticeable local variations in the thickness of the W and Mo marker layers. The latter may be connected with inhomogeneities in the thickness profiles of the markers but equally well to a poor statistical significance of data extracted from cross sections with a limited length. In any case, the data prove that the SIMS results discussed in section 3.1.2 cannot reveal the full layered structure of the deposits even if they correctly predict B-rich parts to be located towards the top.

On the *thick deposits* (example in Fig. 5(b1) taken from s = 180.5 mm), a zoo of different structures can be recognized. These range from stratified but porous deposits, consisting of multiple sublayers, to flakes, sheets, and micrometre-sized particulates around which new sublayers have started to grow. Large inhomogeneities are present at the microscopic scale whereas at the interfaces between the marker layers and the deposits, cracks and local delamination are evidenced. Of the sublayers, some are rich in B and C (like point #2) while the others are more homogeneous mixtures of B, C, N, O, and W (e.g., point #1). Deeper inside, the composition of the individual layers changes towards oxidized W or structures where different metallic elements, dominantly Cu, are more or less equally abundant in addition to the light impurities B, C, and O (point #3). Segregation of the different elements in zones is apparent (see Fig. 5(b2) for corresponding spectra from “light” and “dark” areas of the C5 sample) as well as transformation of the amorphous material into more crystalline type of structures in places with signs of overheating. The longer the exposure time, the thicker and the more complex the deposits have evolved but generally the pattern is similar to what has been concluded in [7] after C3 and C4. The complexity of the structures and rapidly changing sublayer configuration shows that methods with

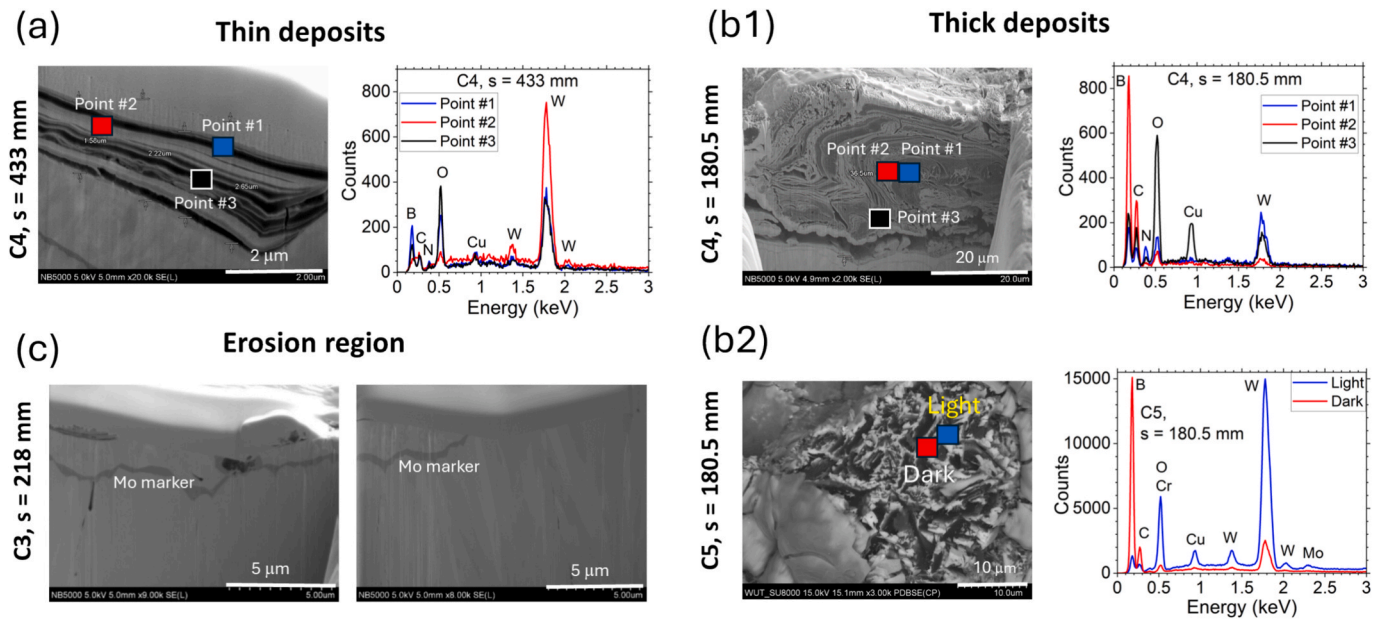

Fig. 5. SEM and EDX images taken from the region of (a) thin (C4, s = 433 mm) and (b1-b2) thick deposits (C4, s = 180.5 mm in (b1); C5, s = 180.5 mm in (b2)) as well as (c) from the erosion-dominated zone (C3, s = 218 mm). In (b2), segregation of different elements is apparent. From the erosion region, the measurements are taken from two adjacent spots. In all cases, the surface is covered with a protective W layer to protect the co-deposit from sputtering during the necessary ion-milling stage.

limited depth and spatial resolution will result in signals from narrow layers becoming fully merged (like is the case for SIMS, GDOES, NRA/RBS, or LIBS), thus they have to be complemented by more local microscopy analyses.

In *erosion areas*, cross sectional images draw a picture consistent with the conclusions from SIMS, GDOES, and LIBS measurements. Only remnants of deposits are visible but considerable erosion can be evidenced, however, with strong local variations. These variations are the most apparent around the ISP (see Fig. 5(c) for the images at $s = 218$ mm) where laterally in the sub-mm scale strong erosion (image on the right) alters with the formation of measurable deposits (image on the left). With increasing plasma exposure (after C4 and C5), all the features become more amplified: erosion down to the substrate and deposits reaching thicknesses of >10 µm and showing many characteristics identical to those of the thick deposits. EDX indicates the most abundant elements in the most strongly eroded regions being B, C, O, and W while next to them the deposits can be even richer in B and O, confirming the analysis performed in [7]. One should note that FIB cross sectional analyses from the OSP region is limited, thereby direct comparison between SEM/EDX and SIMS analyses has to be taken with caution.

The observed structures are similar to those found in ASDEX Upgrade [20,21] thus proving that in similar exposure conditions comparable deposited layers are formed independently of which tungsten device is considered.

3.3. Composition of the deposited layers

The SIMS measurements can also be used to obtain qualitative information on the deposition of different light elements (D, B, and C) poloidally on the analysed samples at a high depth resolution within the surface layers. In the case of the thickest deposits, SIMS is also able to probe deeper than is the case for standard NRA (see [5,7]). Besides results discussed in the preceding sections, a series of XPS measurements were performed at selected poloidal locations to determine the composition of the very surface (down to the beforementioned 5–10 nm) as well as EDX analyses for the extracted SEM images to obtain corresponding elemental information much more locally than is the case for XPS. Both in XPS and EDX, the focus was put on the B, O, and W contents of the surface films (converted into at.%).

The integrals over the B, C, and D deposition peaks in the SIMS depth profiles are shown in Fig. 6(a)-(c), respectively. The numbers on the left-hand side axis have been obtained by using the NRA data from the very same samples as a reference for fitting (axis on the right). This way, parts from (a) to (c) become directly comparable. The results from XPS and EDX compositional analyses are collected in Fig. 6(d)-(f), separately for B, O, and W, respectively. In addition, average concentrations from the reconstructed NRA/RBS depth profiles are included in the graphs.

Concerning B, the profile in Fig. 6(a) peaks at the HFS around the thick deposits, similarly to what has been published in [5,7]. Somewhat contrary to NRA measurements from full tiles, B levels appear to be the highest after C4 but this could be explained by the different analysis depths of the two techniques and the fact that the NRA results have to be extrapolated throughout the entire thickness of the deposit with constant values beyond the measurement limit as stated in section 2.3 to result in fully comparable values to those given by SIMS. The same rationale can explain why the XPS and EDX patterns differ largely from each other: XPS gives information only from the topmost few atomic layers while EDX extends much deeper. On the other hand, due to the local nature of EDX analyses, the absolute values differ greatly from one measurement to another. NRA gives the highest estimates for the elemental B concentrations, most probably because of the largest analysis volume applied.

For the other elements, similarities and differences between the SIMS and published NRA data are evident. The C profile is consistent with the results in [5,7] while for D discrepancies are present in the HFS, particularly for the thick deposits ($s = 100$–200 mm). As discussed in section 3.1, this can be due to local variations in the detailed composition of the thick surface layer, but also the different analysis depths and lateral resolutions for the various analysis methods play a role. Finally, one should not forget that the thick deposits are often badly damaged, even partly peeled off from their substrates, which induces severe uncertainties for any sequential set of analyses performed. The O levels are generally higher than the C concentrations and can lie around 15–40 at.%; The NRA values are closest to the lower limit, while the XPS estimates even exceed 40 at.%. These are some 2–3 times larger than what is the case for B (typically 10–30 at.%) but also for W in the regions of thin/

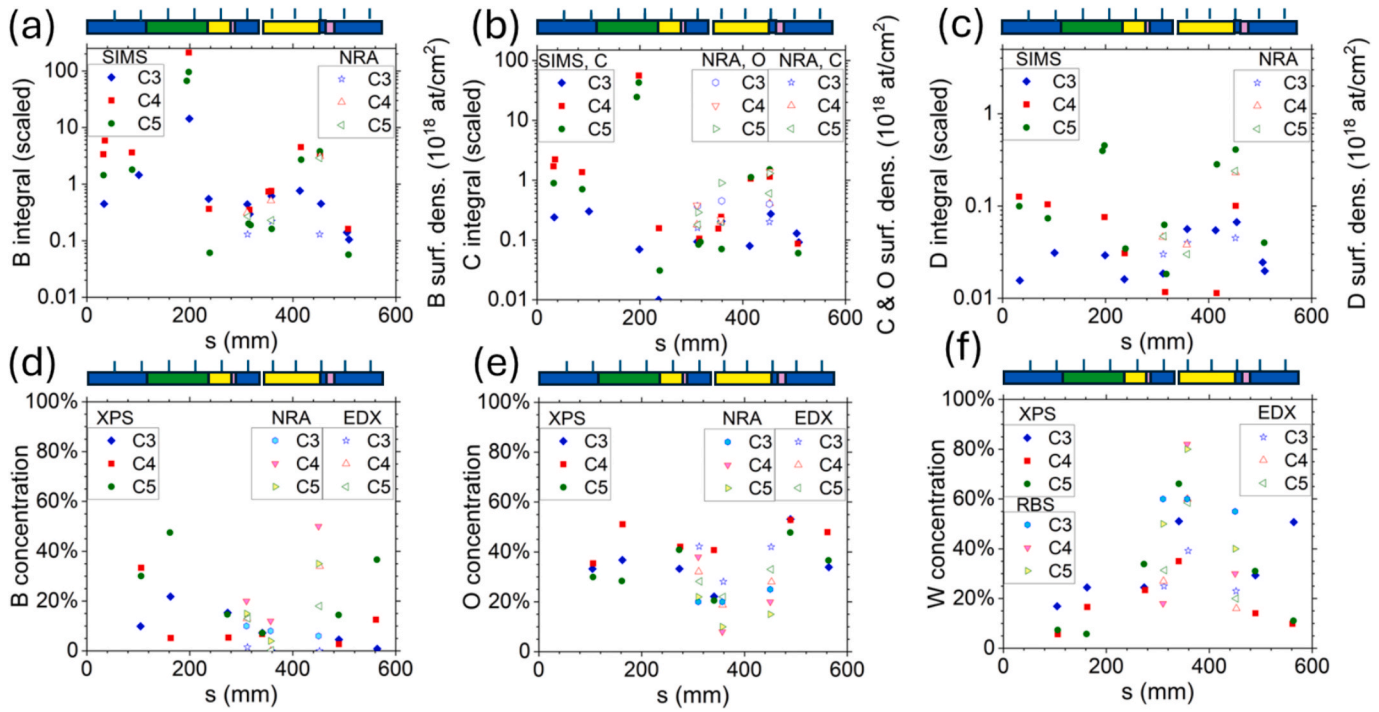

Fig. 6. (a-c) Poloidal deposition profiles, based on SIMS (left y axis) and NRA (right y axis) data, for (a) boron, (b) carbon and oxygen, and (c) deuterium. Notice the different y axis scaling for part (c). (d-f) Elemental concentrations in the surface layers in the poloidal direction, extracted from EDX, NRA/RBS, and XPS measurements, for (d) boron, (e) oxygen, and (f) tungsten. The color coding for the different characteristic regions is the same as in Fig. 3. The different s coordinate values result from applying different techniques for different core-drilled samples according to Table 2.

thick deposits (generally $<$ 20 at.%). In the net-erosion zone, the W levels vary from lowish values (comparable to the results for thin deposits) to higher ones (60–80 at.%) at the OSP; Again the highest values result from ion-beam measurements. The results indicate that even on erosion-dominated regions a thin re-deposited layer can be grown, though not as a continuous film but concentrated inside recessed valleys of the surface, while the largest W values are indicative of a surface where oxidized W is predominantly present.

4. Discussion and conclusions

In this article, we have discussed the detailed elemental, compositional, and structural characteristics of co-deposited layers formed on the PFCs at the divertor region of the WEST tokamak during its Phase 1 plasma operations. The investigations were facilitated by special marker PFCs, sequentially removed for surface analyses from the inner and outer divertor regions after the C3, C4, and C5 experimental campaigns.

The thickest deposits formed towards the end of Phase 1 and the change was particularly noticeable during C4. This can be attributed to the extended exposure of the divertor PFCs to high heating powers in varying plasma scenarios as well as to the large number of boronizations carried out. The previously identified characteristic poloidal regions – thin deposits, thick deposits, and erosion zones – were confirmed by our analyses and the results agreed with the published data [5,7]. Particularly noteworthy are the strong local variations in the properties of the thickest surface deposits both in the toroidal and poloidal directions as well as their strongly layered structure poloidally throughout the entire divertor. Different analysis methods gave largely consistent information, however, some discrepancies were unavoidable due to the varying analysis volumes, both laterally and along the depth direction. Moreover, even if many of the applied techniques allowed obtaining information from the entire pile of material accumulated on the PFCs, their depth resolutions quickly degraded due to the rapidly varying layered structure in the μm scale and lateral inhomogeneities in the sub-mm range once probing deeper from the surface.

The thin deposits showed distinct sublayers rich in B, C, O, and/or W but also metallic impurities such as Ni, Fe, Cu, and Mo together with these main constituents. The thick deposits, in contrast, exhibited a much more complex, stratified structure, yet, regions dominated by the presence of B or W could still be recognized. The very surface appeared to be rich in B in the case of thin deposits while for the thick deposits W was more abundant in the topmost parts of the structure. The average B and W contents inside the thin or thick deposits were consistently in the range 10–30 at.%, with the B concentrations tending to increase with decreasing thickness of the deposits on the SOL side while more W was present in the PFR. In the erosion-dominated regions, the deposits were typically very thin, however, in particular inside recessed valleys, layers up to some micrometers were measured. This can explain why many of the analysis techniques indicated measurable B concentrations in these areas. Oxygen levels could reach values up to 20–40 at.% in the deposits throughout the entire surface layer. A dynamical erosion–deposition picture could be identified, evident from the fact that the deposits did not show an ever thickening pile of layers that could be associated in a straightforward manner with a specific experiment or operational phase of WEST. A caveat, however, is that the results were not always reflecting the full exposure history but dominated by phases with the largest amount of fluence accumulated.

Our results provide further insights into the erosion–deposition picture on WEST PFCs by presenting and comparing data taken by a variety of analysis methods, thereby at different depth resolutions. We have demonstrated that during plasma operations in fusion reactors, determining the balance between the different phenomena – including gross and net erosion – requires taking the full dynamics of subsequent plasma operations into account.

CRediT authorship contribution statement

A. Hakola: Writing – review & editing, Writing – original draft, Visualization, Methodology, Investigation, Formal analysis, Data curation, Conceptualization. **J. Likonen:** Investigation, Data curation. **T.**

Vuoriheimo: Formal analysis. **E. Grigore:** Validation, Data curation. **I. Jõgi:** Writing – review & editing, Investigation, Formal analysis, Data curation. **P. Paris:** Writing – review & editing. **A. Lagoyannis:** Investigation. **K. Mergia:** Writing – review & editing, Data curation. **P. Tsavalas:** Investigation. **E. Fortuna-Zaleśna:** Writing – review & editing, Investigation, Formal analysis, Data curation. **M. Balden:** Writing – review & editing, Data curation. **E. Bernard:** Project administration. **M. Diez:** Writing – review & editing, Project administration, Data curation. **E. Tsitrone:** Supervision.

Declaration of competing interest

The authors declare the following financial interests/personal relationships which may be considered as potential competing interests: Antti Hakola reports financial support was provided by European Consortium for the Development of Fusion Energy. If there are other authors, they declare that they have no known competing financial interests or personal relationships that could have appeared to influence the work reported in this paper.

Acknowledgement

This work has been carried out within the framework of the EUROfusion Consortium, funded by the European Union via the Euratom Research and Training Programme (Grant Agreement No 101052200 — EUROfusion). Views and opinions expressed are however those of the author(s) only and do not necessarily reflect those of the European Union or the European Commission. Neither the European Union nor the European Commission can be held responsible for them.

Data availability

Data will be made available on request.

References

[1] R.A. Pitts, et al., Plasma Phys. Control. Fusion 47 (2025) B303.
[2] S. Brezinsek, et al., J. Nucl. Mater. 463 (2015) 11.
[3] A. Hakola, et al., Nucl. Fusion 61 (2021) 116006.
[4] W. Zheng, et al., Nucl. Mater. Energy 41 (2024) 101828.
[5] M. Diez, et al., Nucl. Mater. Energy 34 (2023) 101399.
[6] J. Bucalossi, et al., Nucl. Fusion 64 (2024) 112022.
[7] M. Balden, et al., Phys. Scr. 96 (2021) 124020.
[8] J. Bucalossi, et al., Nucl. Fusion 62 (2022) 042007.
[9] E. Tsitrone, et al., Nucl. Fusion 62 (2022) 076028.
[10] C. Martin, et al., Phys. Scr. 96 (2021) 124035.
[11] I. Jõgi, et al., J. Nucl. Eng. 4 (2023) 96.
[12] C. Martin, et al., Nucl. Mater. Energy 41 (2024) 101764.
[13] M. Balden, Erosion and redeposition patterns on divertor tiles after exposure in the first operation phase of WEST, this conference.
[14] M. Firdaouss, et al., Fusion Eng. Des. 124 (2017) 207.
[15] S. Lehto, et al., Fusion Eng. Des. 66–68 (2003) 241.
[16] A. Hakola, et al., Plasma Phys. Control. Fusion 52 (2010) 065006.
[17] C. Ruset, et al., Nucl. Mater. Energy 30 (2022) 101151.
[18] P. Tsavalas, et al., Nucl. Fusion 62 (2022) 126070.
[19] I. Jõgi et al., Ex-situ LIBS study for the determination of boron content in WEST divertor tiles after the 2019 campaign, this conference.
[20] E. Fortuna-Zalesna, et al., Phys. Scr. T159 (2014) 014066.
[21] E. Fortuna-Zalesna, et al., Nucl. Mater. Energy 9 (2016) 128.
[22] R. Mateus et al., Elemental analysis of divertor marker tiles exposed during the 2018 (C3), 2019 (C4) and 2020 (C5) WEST campaigns, this conference.